Article

Bolometer operating at the threshold for circuit quantum electrodynamics

R. Kokkoniemi[1,5,9], J.-P. Girard[1,9], D. Hazra[1,2], A. Laitinen[3,6], J. Govenius[1,2], R. E. Lake[1,7], I. Sallinen[1], V. Vesterinen[1,2], M. Partanen[1,8], J. Y. Tan[4], K. W. Chan[4,5], K. Y. Tan[1,5], P. Hakonen[3] & M. Möttönen[1,2 ✉]

Radiation sensors based on the heating effect of absorbed radiation are typically simple to operate and flexible in terms of input frequency, so they are widely used in gas detection[1], security[2], terahertz imaging[3], astrophysical observations[4] and medical applications[5]. Several important applications are currently emerging from quantum technology and especially from electrical circuits that behave quantum mechanically, that is, circuit quantum electrodynamics[6]. This field has given rise to single-photon microwave detectors[7–9] and a quantum computer that is superior to classical supercomputers for certain tasks[10]. Thermal sensors hold potential for enhancing such devices because they do not add quantum noise and they are smaller, simpler and consume about six orders of magnitude less power than the frequently used travelling-wave parametric amplifiers[11]. However, despite great progress in the speed[12] and noise levels[13] of thermal sensors, no bolometer has previously met the threshold for circuit quantum electrodynamics, which lies at a time constant of a few hundred nanoseconds and a simultaneous energy resolution of the order of $10h$ gigahertz (where h is the Planck constant). Here we experimentally demonstrate a bolometer that operates at this threshold, with a noise-equivalent power of 30 zeptowatts per square-root hertz, comparable to the lowest value reported so far[13], at a thermal time constant two orders of magnitude shorter, at 500 nanoseconds. Both of these values are measured directly on the same device, giving an accurate estimation of $30h$ gigahertz for the calorimetric energy resolution. These improvements stem from the use of a graphene monolayer with extremely low specific heat[14] as the active material. The minimum observed time constant of 200 nanoseconds is well below the dephasing times of roughly 100 microseconds reported for superconducting qubits[15] and matches the timescales of currently used readout schemes[16,17], thus enabling circuit quantum electrodynamics applications for bolometers.

Extensive research has been carried out on sensitive terahertz detectors such as transition-edge sensors[18] (TESs), kinetic-inductance detectors[19] (KIDs), quantum dots[20] and qubit-based detectors[7–9]. Especially TESs and KIDs have reached technological maturity and are widely applied in astronomy, for example, in observations of the cosmic microwave background[4]. However, detectors used for propagating single microwave photons are still in the early development stage, mainly because the low photon energies (much lower than in terahertz sensing) require higher sensitivity. Qubit-based detectors have been operated in the single-microwave-photon regime but they have a relatively narrow absorption bandwidth, typically of the order of 10 MHz, and a dynamic range limited to a single[7,8] or a few[9] photons. Travelling-wave parametric amplifiers[11] provide gigahertz bandwidth and a large dynamic range,

but quantum noise hinders their operation as single-photon detectors. A broad-band high-fidelity single-photon detector based on a similar technology has been proposed[21], but has not yet been experimentally studied. By contrast, thermal detectors are free of quantum noise, may provide a large detection bandwidth and dynamic range and could even enable an energy-resolving detection mode[22].

Thus, advancing thermal detectors towards the single-microwave-photon regime is of great interest to circuit quantum electrodynamics (cQED). Such detectors have applications in quantum illumination[23,24], parity measurement[25] and qubit readout[26,27], where their readout frequency can be engineered independently of the detection frequency, possibly alleviating frequency crowding in large-scale multiplexing of qubit readout signals; qubit readout

[1]QCD Labs, QTF Centre of Excellence, Department of Applied Physics, Aalto University, Espoo, Finland. [2]VTT Technical Research Centre of Finland Ltd, QTF Centre of Excellence, Espoo, Finland. [3]Low Temperature Laboratory, QTF Centre of Excellence, Department of Applied Physics, Aalto University, Espoo, Finland. [4]Centre for Advanced 2D Materials and Graphene Research Centre, National University of Singapore, Singapore, Singapore. [5]Present address: IQM, Espoo, Finland. [6]Present address: Department of Physics, Harvard University, Cambridge, MA, USA. [7]Present address: Bluefors Oy, Helsinki, Finland. [8]Present address: Walther-Meißner-Institut, Bayerische Akademie der Wissenschaften, Garching, Germany. [9]These authors contributed equally: R. Kokkoniemi, J.-P. Girard. ✉e-mail: mikko.mottonen@aalto.fi
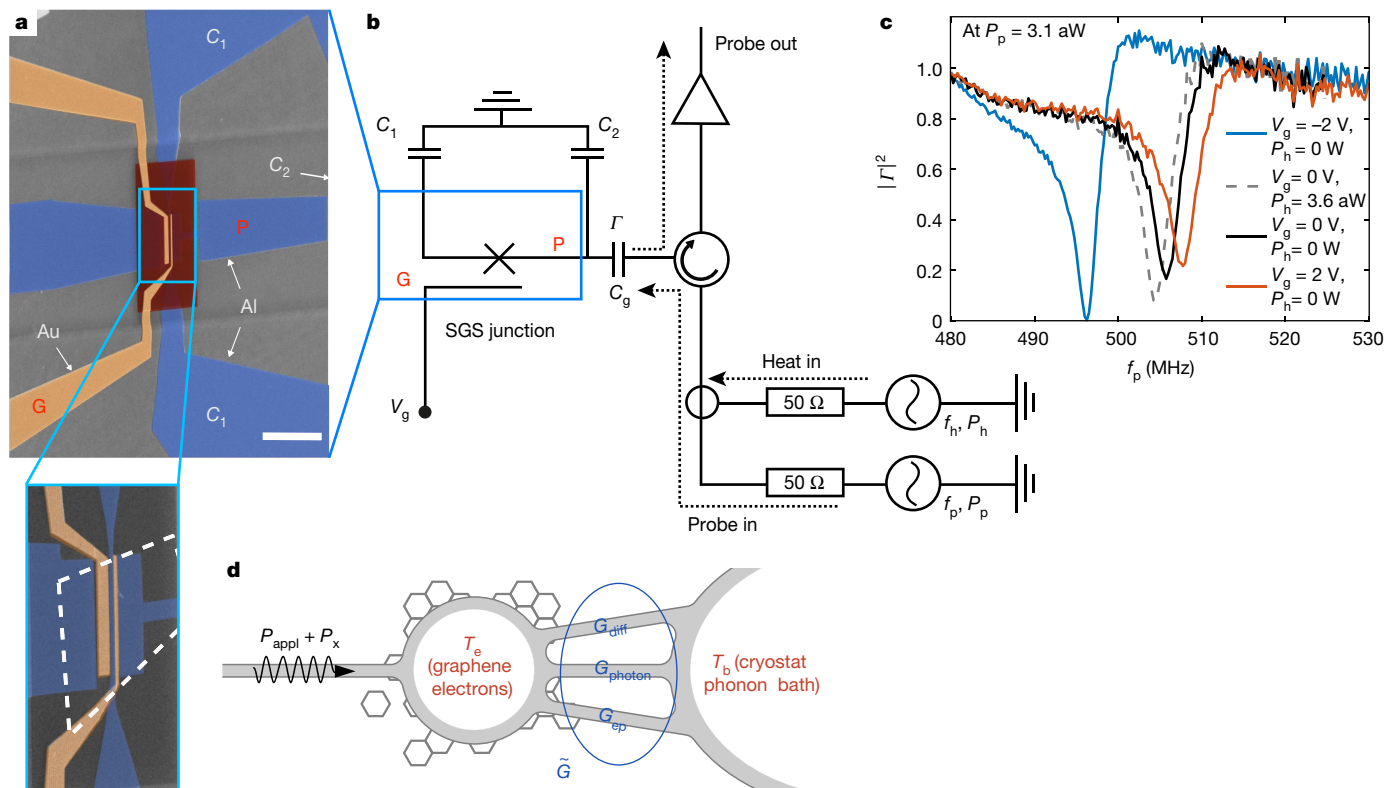
Fig. 1 | Bolometer and its operation principle. a, False-colour scanning electron microscope (SEM) image of the graphene bolometer. The scale bar denotes 10 μm. The gate voltage is applied on port G, whereas the heater and probe signals couple through port P to the SGS junction formed between the aluminium (blue colour) electrodes of port P and of the capacitor C_1. The extent of the graphene flake is indicated by the white dashed line in the inset, where we do not show the gate insulator (red colour) for clarity. See Extended Data Figs. 3, 7 for more details. The leftmost aluminium and gold (orange colour) electrodes are not used in this work. **b**, Circuit diagram of the detector and a simplified measurement setup. The heater and probe signals (denoted by subscripts h and p, respectively) are combined at room temperature. The microwave reflection coefficient for the probe tone is denoted by Γ. **c**, Reflected fraction of the probe power P_p as a function of the probe frequency f_p for the indicated gate voltages V_g and heater powers P_h at a bath temperature of $T_b = 55$ mK. **d**, Considered thermal model. The electrons in the graphene are coupled to the cryostat phonons through an effective thermal conductance of $\widetilde{G} = G_{ep} + G_{diff} + G_{photon}$, which is a sum of the phononic (G_{ep}), electron diffusion (G_{diff}) and photonic (G_{photon}) thermal conductances (see Methods).

signals even at equal carrier frequencies may be detected by an array of bolometers using frequency multiplexing in its readout. In entanglement experiments, photon number eigenstates and their detection[28] offer advantages over homodyne techniques, for example, in mitigating photon loss[29,30]. Furthermore, thermal detectors operating at millikelvin temperatures may decrease the overhead related to the characterization of microwave components[31,32] at the single-photon regime, a task that requires a sophisticated amplification chain and its calibration in the case of room-temperature detectors. Such a characterization is necessary for many components operated at ultralow powers, for example, in quantum computers.

Radiation detectors are often characterized in terms of noise-equivalent power (NEP); that is, the noise in the readout signal, in units of the input power of the detector. Mature technologies such as TESs and KIDs have been able to reach NEPs in range of a few hundred zW Hz$^{-1/2}$. We recently introduced a Josephson junction-based bolometer[13,33] with NEP = 20 zW Hz$^{-1/2}$ when operated with a near-quantum-limited amplifier[34]. Furthermore, qubit-based quantum capacitance sensors[35] have recently been reported to have an NEP below 10 zW Hz$^{-1/2}$. Even lower NEP is expected from semiconducting charge sensors[36], but full experimental characterization is lacking. Recently, a superconductor–normal–metal calorimeter reached the limit of fundamental temperature fluctuations in thermometry, which is promising for detection of single microwave photons[37].

Sensitive bolometry typically relies on maximizing the temperature changes from photon absorption. To this end, one may minimize the absorber volume, use materials of low specific heat and decrease the thermal conductance of the absorber to increase the low-frequency response. Graphene has a low electron density of states, leading to a low heat capacity and a fast response, which are desirable for single-microwave-photon bolometers. At 5 K, an extremely short thermal relaxation time of 35 ps has been reported[12] for a graphene-based bolometer. Another recent study on a graphene–Josephson junction-based bolometer[38] carried out at 0.19 K predicts an NEP of 700 zW Hz$^{-1/2}$ and an energy resolution as low as $32h$ GHz, but does not report a measured thermal time constant, so these results remain to be verified experimentally (Supplementary Note I, Supplementary Table S1, Supplementary Figs. S2–S5). Importantly, the resistance of graphene absorbers can be tuned by an electric field, which allows precise impedance matching with an antenna or a waveguide using, for example, the detector design of refs. [13,33].

Here, we introduce and demonstrate a hot-electron bolometer based on a superconductor–graphene–superconductor (SGS) junction (Fig. 1a). We couple this junction to on-chip capacitors forming a temperature-dependent LC oscillator (Fig. 1b). Incident radiation absorbed in the graphene modifies the resonance frequency of the oscillator, which serves as our thermometer. For example, Fig. 1c shows a megahertz-level redshift for a heater power of a few attowatts.
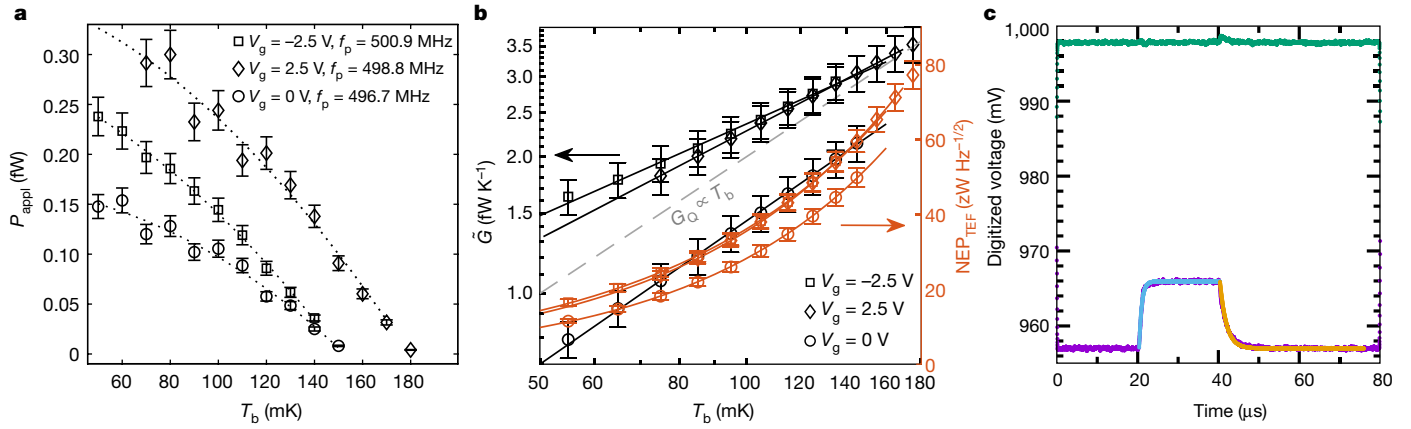
Fig. 2 | Sample characterization data. a, Measured points of constant resonance frequency (markers) in the plane of the cryostat phonon temperature, T_b, and the absorbed power in the graphene, P_{appl}, for the indicated gate voltages and probe frequencies. The dotted lines represent polynomial fits to the data (see Extended Data Table 1 for parameter values). **b**, Differential thermal conductance of the graphene electron system (black markers), $\widetilde{G}$, as a function of T_b, obtained by differentiating the polynomial fits in **a** with respect to T_b at the temperature points of the measured data. The black solid lines are fits to the data, and are linear on a logarithmic scale. The grey dashed line shows 2.0% of the quantum of the thermal conductance G_Q.

The red markers and lines show the thermal-fluctuation-limited NEP, NEP_{TEF} (right vertical axis) corresponding to the differential thermal conductance shown in black. The error bars in **a** and **b** denote 1σ confidence intervals. **c**, Example time trace of the in-phase (purple markers) and quadrature (green markers) voltage of the measured probe signal for the case in which the heater power is quickly turned on at time $t = 20\,\mu s$ and turned off at $t = 40\,\mu s$. An exponential fit to the rising edge of the real part is denoted with cyan and a fit to the falling edge with orange. The thermal time constant and the quasistatic response of the bolometer is obtained from the fits.

The properties of the detector can be tuned by the electric field induced by a gate on the SGS junction and by the power and frequency of the probe signal. The LC resonance frequency changes by roughly 80 MHz (see Extended Data Fig. 1), and the thermal time constant varies from 200 ns to several microseconds with the probe power and electric field. Optimization yields a low NEP of 30 zW Hz$^{-1/2}$ at a thermal time constant of 500 ns. These results indicate an energy resolution as low as $30h$ GHz. Importantly, we obtain the NEP and the time constant from direct measurements. Our device shows a weak thermal energy exchange with its environment, with a differential thermal conductance between the graphene bolometer and the phonon bath of the cryostat as low as 0.8 fW K^{-1}, which is less than 2% of the quantum of thermal conductance G_Q at 50 mK.

The steady-state thermal power from the electrons in the graphene (temperature T_e) to the cryostat bath (T_b) equals $P_{eb}(T_e, T_b) = P_{appl} + P_x$, where P_x denotes parasitic heating, $P_{appl} = (1 - |\Gamma|^2)P_p$ is the probe power absorbed by graphene, Γ is the reflection coefficient at the gate capacitor C_g (see Fig. 1b) and P_p is the probe power incident on the capacitor. We define the differential thermal conductance as

$$\widetilde{G} = -\partial P_{eb}(T_e, T_b)/\partial T_b$$

and measure it by changing the bath temperature, and compensating for the resulting change in the resonance frequency—and hence the electron temperature—by changing the applied power as shown in Fig. 2a. Because the electron temperature is constant, the change in the applied power fully flows to the bath, and hence we obtain $\widetilde{G}$ in Fig. 2b as the derivative of the applied power with respect to the bath temperature from Fig. 2a. We observe that $\widetilde{G}$ scales at most linearly with T_b, as does the quantum of thermal conductance $G_Q = \pi^2 k_B^2 T_b/(3h)$, where k_B is the Boltzmann constant. This scaling is considerably weaker than that reported for electron–phonon coupling in monolayer graphene in refs. [39–43], where $\widetilde{G} \propto T_b^\delta$ with $\delta \approx 2$–4. This discrepancy suggests that phononic coupling is not dominant in our sample. Our observations are also unlikely to arise from electron diffusion because the superconducting leads to the graphene flake suppress this effect[44]. Multiple Andreev reflections may contribute to the heat conduction

through the leads[45], but their effect is greatly suppressed at the applied vanishing voltage bias across the SGS junction.

However, the observed linear temperature dependence of $\widetilde{G}$ may be explained by photonic coupling $G_{photon} \propto T_b$ (ref. [46]). This photonic thermal conductance should dominate over the electron–phonon coupling below the crossover temperature[47] $T_{cr} = \left[r_0 \pi^2 k_B^2 \big/ (15h\Sigma S_{graphene}) \right]^{1/2}$, where r_0 quantifies the impedance matching between the detector and its electromagnetic environment, the electron–phonon coupling constant Σ is characteristic for the material and $S_{graphene}$ is the area of the electron gas. Considering a typical value[48] for graphene of $\Sigma = 10^{-15}$ W μm^{-2} K^{-4} and an impedance matching of $r_0 > 10^{-2}$, corresponding to a maximum isolation of 1% of the quantum of thermal conductance (see Fig. 2), one obtains $T_{cr} \gtrsim 300$ mK. Thus, photonic coupling is probably dominating in our temperature range below 200 mK.

We evaluate the NEP as the voltage noise in the readout signal divided by the voltage responsivity of the detector to the absorbed power. For convenience, we measure only the quasistatic responsivity and divide it by $\sqrt{1 + (2\pi\tau f_n)^2}$, which takes into account the thermal cut-off in the responsivity for noise frequencies f_n higher than the inverse thermal relaxation time $1/\tau$. This is a generally accepted method with which to obtain the responsivity, justified here by our observations of exponential thermal relaxation dominated by a single time constant (see Fig. 2c). Extended Data Fig. 2 shows the measured response and voltage noise.

Figure 3a–c shows the experimentally obtained NEP and time constant as functions of the probe frequency at different gate voltages. The minimum NEP = 30 zW Hz$^{-1/2}$ occurs at gate voltage $V_g = 0$ V and probe frequency $f_p = 503$ MHz, where the thermal time constant is $\tau = 500$ ns. The minimum observed time constant is 200 ns. Although $1/\tau$ yields the speed of the energy relaxation of the bolometer, it does not pose a fundamental limitation on the speed of detecting energy packets. Namely, if the internal thermalization of the electrons in the bolometer is fast, the rising edge of the readout signal can be orders of magnitude shorter than the falling edge set by τ. Thus, the measured time constant seems promising for cQED applications with readout times of the order of 100 ns.

Random exchange of energy quanta between a bolometer and its environment induces fluctuations in the electron temperature, and
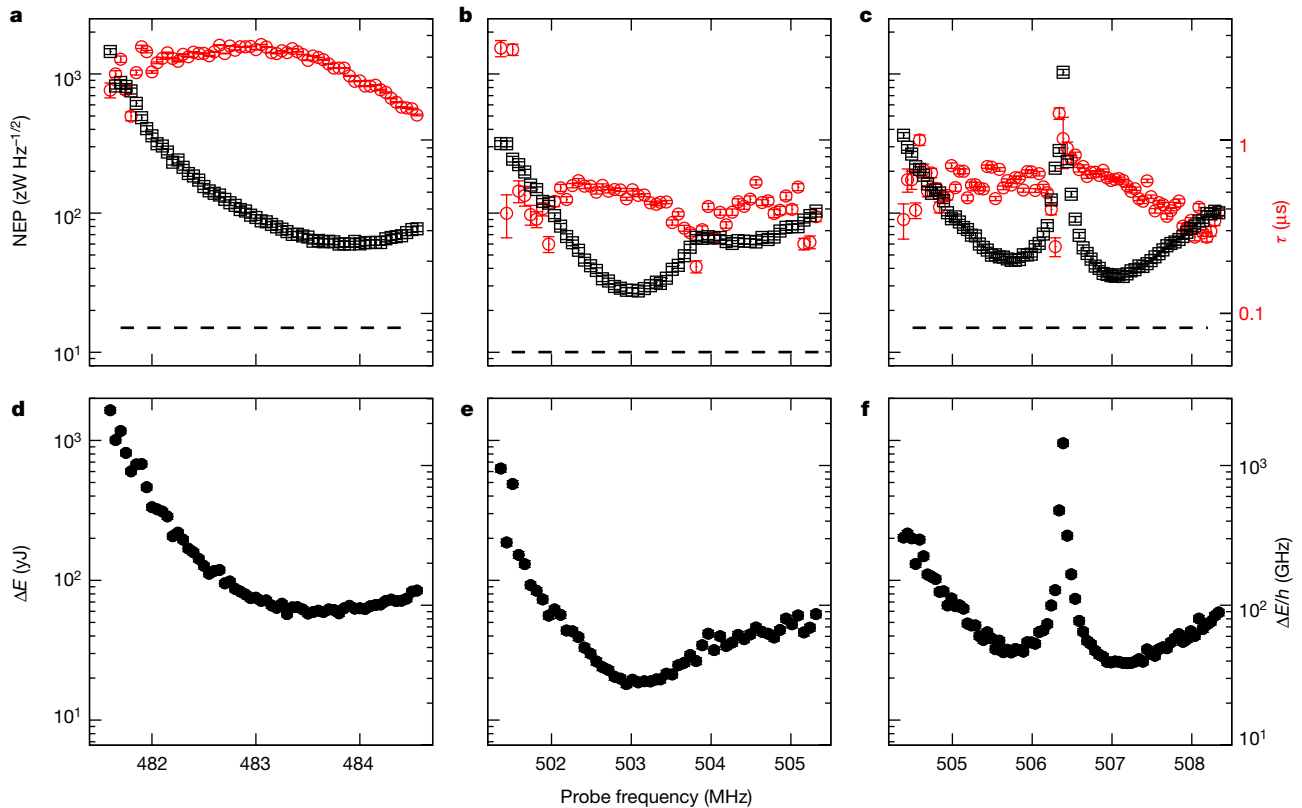
Fig. 3 | Key performance indicators of the bolometer. a–c, Measured NEP (black markers, left axis) and thermal relaxation time τ (red markers, right axis) of the detector for gate voltages $V_g = -2.5\,V$ (**a**), $V_g = 0\,V$ (**b**) and $V_g = 2.5\,V$ (**c**), bath temperature $T_b = 55\,mK$ and probe power $P_p = 530\,aW$ (**a**), $P_p = 140\,aW$ (**b**) and $P_p = 370\,aW$ (**c**). The dashed horizontal lines indicate the thermal-fluctuation-limited NEPs obtained from the thermal conductance given in Fig. 2b. The error bars denote 1σ confidence intervals. **d–f,** Energy resolution of the bolometer obtained from the NEP and τ results of panels **a–c,** respectively. The error bars, which are smaller than the marker size, denote 1σ confidence intervals.

hence noise[37]. The thermal-fluctuation-limited NEP is given by[49] $NEP_{TEF} = \sqrt{4k_B T_e^2 \widetilde{G}}$. Using $T_e = 55\,mK$ and $\widetilde{G} = 0.8\,fW\,K^{-1}$ from Fig. 2b, we obtain $NEP_{TEF} = 12\,zW\,Hz^{-1/2}$. This indicates that our bolometer operates close to the thermal bound. Thus, improvements of roughly a factor of two in the minimum NEP may be achievable by technical changes to the measurement setup, as was obtained in ref. [13] by introducing a near-quantum-limited amplifier. However, major progress requires further development of the bolometer, such as redesign of the sample or use of new materials. Reduction of the photonic heat conduction by advanced shielding and filtering may improve the NEP.

We extract the energy resolution using the NEP[50], $\Delta E = \left(\int_0^\infty \frac{4\,df_n}{NEP(f_n)^2} \right)^{-1/2}$, and show the results in Fig. 3d–f. The finest energy resolution of $20\,yJ = 30h\,GHz$ ($1\,yJ = 10^{-24}\,J$) appears at 55 mK. This corresponds to the energy of five 6-GHz photons, which is a suitable frequency and photon number scale for the usual[16] and multichannel[17] readout of superconducting qubits. The bolometer also seems like an ideal detector candidate in the alternative qubit readout scheme demonstrated in ref. [27], where the total energy at the first-stage measurement device may be high, for example, $100\,yJ = 150h\,GHz$.

Thus, the obtained fine energy resolution and simultaneous fast response meet the threshold for some applications in cQED that use ultralow powers and enable detection in timescales that are orders of magnitude shorter than the typical state-of-the-art coherence times of roughly 100 μs (ref. [15]). The exact performance level required to meet the threshold depends on the application and is of the order of $10h\,GHz$ and 100 ns for typical qubit readout schemes, as discussed above. There are various other requirements and desired properties for devices operating in cQED, such as small size, low power dissipation, robustness to

electric and magnetic noise and low backaction. Our bolometer seems promising in this respect thanks to its micrometre-sized detection element, below-picowatt probe power, high electric and magnetic fields required to shift the resonance, and flexibility in choosing a probe frequency far from the detection frequency (see ref. [33]), providing good isolation of these two signals, for example, 80 dB using a first-order band-pass filter.

A thermal model with a single thermal relaxation time (see Fig. 1d) is enough to describe our observations. Therefore, we can estimate the heat capacity of the graphene as $C_e = \widetilde{G}\tau$. Because electrothermal feedback affects the measured time constant[33], we use $\tau = 300\,ns$ from Fig. 3b to avoid artificially decreasing the estimated heat capacity. Together with the measured $\widetilde{G} = 0.8\,fW\,K^{-1}$, we obtain $C_e = 2.5 \times 10^{-22}\,J\,K^{-1}$, which corresponds to $1.2 \times 10^{-23}\,J\,K^{-1}\,\mu m^{-2} = 0.87k_B\,\mu m^{-2}$. This is in good agreement with the literature value of roughly $2k_B\,\mu m^{-2}$ at 50 mK, assuming a linear temperature dependence of the heat capacity[14]. Consequently, we obtain the standard deviation of the energy due to fundamental thermal fluctuations $\Delta E_{th} = \sqrt{k_B T_e^2 C_e} = 3\,yJ = 4.4h\,GHz$ at 50 mK.

This study experimentally demonstrates an ultrafast low-noise graphene bolometer operating in the microwave range, with a measured thermal conductance as low as $0.8\,fW\,K^{-1}$, a thermal relaxation time of $\tau = 200\,ns$ and $NEP = 30\,zW\,Hz^{-1/2}$, which is close to the corresponding thermal-fluctuation limit, $NEP_{TEF} = 12\,zW\,Hz^{-1/2}$. At the most sensitive operation point, our estimates for the bounds from other noise sources include that of the Johnson noise radiating from the junction to the amplification chain (~1 zW Hz$^{-1/2}$), amplifier noise (~4 zW Hz$^{-1/2}$) and fluctuations of the SGS temperature due to shot noise of photons absorbed from the probe tone (~7 zW Hz$^{-1/2}$). An integration of a near-quantum-limited amplifier to the amplification chain[13] has the

potential to eliminate the latter two contributions by using a device identical to that presented here. Our experiments indicate an energy resolution of $30h$ GHz, which is, to the best of our knowledge, the finest resolution reported for a thermal detector. Interestingly, the estimated low heat capacity of the bolometer implies a thermal energy uncertainty of only $4.4h$ GHz, which suggests that the energy resolution of a single excitation in typical cQED devices may be achievable by technical improvements in the measurement setup, such as expansion of the readout bandwidth. In the future, we aim to use bolometers to study cQED using photon-number-based detection, free of quantum noise stemming from the Heisenberg uncertainty relations.

Online content

Any methods, additional references, Nature Research reporting summaries, source data, extended data, supplementary information, acknowledgements, peer review information; details of author contributions and competing interests; and statements of data and code availability are available at https://doi.org/10.1038/s41586-020-2753-3.

1. Harmon, S. A. & Cheville, R. A. Part-per-million gas detection from long-baseline THz spectroscopy. *Appl. Phys. Lett.* **85**, 2128–2130 (2004).
2. Woodward, R. M. Terahertz technology in global homeland security. *Proc. SPIE* **5781**, 22–31 (2005).
3. Woolard, D. L., Brown, E. R., Pepper, M. & Kemp, M. Terahertz frequency sensing and imaging: a time of reckoning future applications? *Proc. IEEE* **93**, 1722–1743 (2005).
4. Stevens, J. R. et al. Characterization of transition edge sensors for the Simons observatory. *J. Low Temp. Phys.* **199**, 672–680 (2020).
5. Pickwell, E. & Wallace, V. P. Biomedical applications of terahertz technology. *J. Phys. D* **39**, R301–R310 (2006).
6. Blais, A., Girvin, S. M. & Oliver, W. D. Quantum information processing and quantum optics with circuit quantum electrodynamics. *Nat. Phys.* **16**, 247–256 (2020).
7. Besse, J.-C. et al. Single-shot quantum nondemolition detection of individual itinerant microwave photons. *Phys. Rev. X* **8**, 021003 (2018).
8. Kono, S., Koshino, K., Tabuchi, Y., Noguchi, A. & Nakamura, Y. Quantum non-demolition detection of an itinerant microwave photon. *Nat. Phys.* **14**, 546–549 (2018).
9. Dassonneville, R., Assouly, R., Peronnin, T., Rouchon, P. & Huard, B. Number-resolved photocounter for propagating microwave mode. Preprint at https://arxiv.org/abs/2004.05114 (2020).
10. Arute, F. et al. Quantum supremacy using a programmable superconducting processor. *Nature* **574**, 505–510 (2019).
11. Macklin, C. et al. A near–quantum-limited Josephson traveling-wave parametric amplifier. *Science* **350**, 307–310 (2015).
12. Efetov, D. K. et al. Fast thermal relaxation in cavity-coupled graphene bolometers with a Johnson noise read-out. *Nat. Nanotechnol.* **13**, 797–801 (2018).
13. Kokkoniemi, R. et al. Nanobolometer with ultralow noise equivalent power. *Commun. Phys.* **2**, 124 (2019).
14. Fong, K. C. et al. Measurement of the electronic thermal conductance channels and heat capacity of graphene at low temperature. *Phys. Rev. X* **3**, 041008 (2013).
15. Rigetti, C. et al. Superconducting qubit in a waveguide cavity with a coherence time approaching 0.1 ms. *Phys. Rev. B* **86**, 100506 (2012).
16. Walter, T. et al. Rapid high-fidelity single-shot dispersive readout of superconducting qubits. *Phys. Rev. Appl.* **7**, 054020 (2017).
17. Ikonen, J. et al. Qubit measurement by multichannel driving. *Phys. Rev. Lett.* **122**, 080503 (2019).
18. Karasik, B. S., Sergeev, A. V. & Prober, D. E. Nanobolometers for THz photon detection. *IEEE Trans. Terahertz Sci. Technol.* **1**, 97–111 (2011).
19. Mazin, B. A. Microwave kinetic inductance detectors: the first decade. *AIP Conf. Proc.* **1185**, 135–142 (2009).
20. Ikushima, K. et al. Photon-counting microscopy of terahertz radiation. *Appl. Phys. Lett.* **88**, 152110 (2006).
21. Grimsmo, A. L. et al. Quantum metamaterial for nondestructive microwave photon counting. Preprint at https://arxiv.org/abs/2005.06483 (2020).
22. Pekola, J. P. Towards quantum thermodynamics in electronic circuits. *Nat. Phys.* **11**, 118–123 (2015).
23. Tan, S.-H. et al. Quantum illumination with Gaussian states. *Phys. Rev. Lett.* **101**, 253601 (2008).
24. Las Heras, U. et al. Quantum illumination reveals phase-shift inducing cloaking. *Sci. Rep.* **7**, 9333 (2017).
25. Govenius, J., Matsuzaki, Y., Savenko, I. G. & Möttönen, M. Parity measurement of remote qubits using dispersive coupling and photodetection. *Phys. Rev. A* **92**, 042305 (2015).
26. Govia, L. C. et al. High-fidelity qubit measurement with a microwave-photon counter. *Phys. Rev. A* **90**, 062307 (2014).
27. Opremcak, A. et al. Measurement of a superconducting qubit with a microwave photon counter. *Science* **361**, 1239–1242 (2018).
28. Takahashi, H. et al. Entanglement distillation from Gaussian input states. *Nat. Photon.* **4**, 178–181 (2010).
29. Narla, A. et al. Robust concurrent remote entanglement between two superconducting qubits. *Phys. Rev. X* **6**, 031036 (2016).
30. Michael, M. H. et al. New class of quantum error-correcting codes for a bosonic mode. *Phys. Rev. X* **6**, 031006 (2016).
31. Sliwa, K. et al. Reconfigurable Josephson circulator/directional amplifier. *Phys. Rev. X* **5**, 041020 (2015).
32. Kokkoniemi, R. et al. Flux-tunable phase shifter for microwaves. *Sci. Rep.* **7**, 14713 (2017).
33. Govenius, J., Lake, R. E., Tan, K. Y. & Möttönen, M. Detection of zeptojoule microwave pulses using electrothermal feedback in proximity-induced Josephson junctions. *Phys. Rev. Lett.* **117**, 030802 (2016).
34. Vesterinen, V. et al. Lumped-element Josephson parametric amplifier at 650 MHz for nano-calorimeter readout. *Supercond. Sci. Technol.* **30**, 085001 (2017).
35. Echternach, P., Pepper, B., Reck, T. & Bradford, C. Single photon detection of 1.5 THz radiation with the quantum capacitance detector. *New Astron.* **2**, 90–97 (2018).
36. Komiyama, S. Single-photon detectors in the terahertz range. *IEEE J. Sel. Top. Quantum Electron.* **17**, 54–66 (2011).
37. Karimi, B., Brange, F., Samuelsson, P. & Pekola, J. P. Reaching the ultimate energy resolution of a quantum detector. *Nat. Commun.* **11**, 367 (2020).
38. Lee, G.-H. et al. Graphene-based Josephson junction microwave bolometer. Preprint at https://arxiv.org/abs/1909.05413 (2019).
39. Chen, W. & Clerk, A. A. Electron–phonon mediated heat flow in disordered graphene. *Phys. Rev. B* **86**, 125443 (2012).
40. El Fatimy, A. et al. Effect of defect-induced cooling on graphene hot-electron bolometers. *Carbon* **154**, 497–502 (2019).
41. Laitinen, A. et al. Electron–phonon coupling in suspended graphene: Supercollisions by ripples. *Nano Lett.* **14**, 3009–3013 (2014).
42. Song, J. C. W., Reizer, M. Y. & Levitov, L. S. Disorder-assisted electron–phonon scattering and cooling pathways in graphene. *Phys. Rev. Lett.* **109**, 106602 (2012).
43. Betz, A. C. et al. Supercollision cooling in undoped graphene. *Nat. Phys.* **9**, 109–112 (2013).
44. Peltonen, J. T. et al. Thermal conductance by the inverse proximity effect in a superconductor. *Phys. Rev. Lett.* **105**, 097004 (2010).
45. Voutilainen, J. et al. Energy relaxation in graphene and its measurement with supercurrent. *Phys. Rev. B* **84**, 045419 (2011).
46. Schmidt, D. R., Schoelkopf, R. J. & Cleland, A. N. Photon-mediated thermal relaxation of electrons in nanostructures. *Phys. Rev. Lett.* **93**, 045901 (2004).
47. Meschke, M., Guichard, W. & Pekola, J. P. Single-mode heat conduction by photons. *Nature* **444**, 187–190 (2006).
48. Betz, A. C. et al. Hot electron cooling by acoustic phonons in graphene. *Phys. Rev. Lett.* **109**, 056805 (2012).
49. Richards, P. L. Bolometers for infrared and millimeter waves. *J. Appl. Phys.* **76**, 1–24 (1994).
50. Enss, C. *Cryogenic Particle Detection* (Springer, 2005).

Article

Methods

Sample fabrication

First, a commercial 4-inch Si substrate with resistivity exceeding $10\,k\Omega\,cm$ is covered with a 300-nm-thick thermally grown silicon oxide (SiO_x). Then, a 200-nm-thick film of niobium is deposited onto the substrate by d.c. magnetron sputtering. Microwave resonators are fabricated using standard photolithography and reactive ion etching of the niobium film. Subsequently, 50-nm-thick aluminium oxide (AlO_x) is grown by atomic layer deposition, covering the entire wafer. The parallel-plate capacitors are patterned and fabricated using standard electron-beam lithography, aluminium evaporation and lift-off. Here, the AlO_x layer serves as the insulator, separating the Nb ground plane from the top Al electrode that is fabricated simultaneously with the Al capacitor plates.

To prepare the graphene[51] junction onto an individual cleaved bolometer chip, graphene is first exfoliated onto a properly prepared Si/SiO₂ substrate using the Scotch tape method. The monolayer character of the exfoliated flake is verified by measuring a half width of $34\,cm^{-1}$ for the peak from two-dimensional Raman scattering at a wavelength of 633 nm. Using a poly(methyl methacrylate) (PMMA) stamp and micromanipulation techniques, the graphene flake is deposited to the desired location on the bolometer chip[52].

Subsequently, the Ti/Al leads from the graphene to the capacitor plates are defined using an electron-beam evaporator and a PMMA mask. The Cr/Au electrode, which is used to gate the carrier density in the graphene, is separated from the flake by a 150-nm PMMA layer, which is crosslinked using a high electron-beam dose and behaves as a suitable insulator.

This fabrication technique based on individual graphene flakes leads to a relatively low throughput and yield, below 40%. A single working sample selected from three trials is used for all data presented in the main text (see also Supplemetary Notes I, II for data on other samples). However, a lithographic process for graphene (see Supplemetary Note I) is likely to provide substantial improvements to this end.

Sample and measurement setup

Figure 1a shows a coloured SEM image of the nanobolometer. The central element of the bolometer is the graphene flake (total surface area of approximately $21\,\mu m^2$), with the SGS junction located below the gate electrode labelled G and the PMMA layer. The SGS junction is connected to a $50\text{-}\Omega$ aluminium superconducting transmission line through a port labelled P. The SGS junction is capacitively coupled to the ground, and from circuit modelling (see Supplementary Methods I and Supplementary Fig. S1) we estimate its intrinsic inductance to be 2.32 nH for $T_b = 55\,mK$ at low probe power, 0 V gate bias and without heater power (see also Supplementary Note II and Supplementary Fig. S6 for inductance measurements using a multimode resonator). We estimate the capacitances C_1, C_2 and C_g (see Extended Data Fig. 3) from the design parameters to be 124 pF, 57 pF and 1.4 pF, respectively.

For the graphene, we estimate the charge carrier density at vanishing gate voltage, and hence the doping, to be $n_0 = C_i \left| V_g^{Dirac} \right| / e > 3 \times 10^{12}\,cm^{-2}$, where $C_i \approx 2.4 \times 10^{-4}\,F\,m^{-2}$ is the capacitance between the graphene flake and the gold electrode and V_g^{Dirac} is the gate voltage of the Dirac point. A Dirac point implies a minimum in the critical current of the junction, and consequently a maximum in its inductance. This in turn corresponds to a minimum of the observed resonance frequency. Extended Data Fig. 1a suggests that $\left| V_g^{Dirac} \right| > 20\,V$ because we do not clearly observe a minumum in the resonance frequency in the chosen gate voltage regime of $|V_g| < 20\,V$.

The experiments are carried out in a commercial cryostat operating at a temperature of 55 mK. The heater and the probe signal generators are connected at room temperature to a single cable that channels the corresponding microwaves to the bolometer through several filters and attenuators. In our scheme, the function of the heater signal is to heat the SGS junction by photon absorption, whereas the probe signal is mostly reflected off the device, amplified and digitized. A part of the heater signal is also reflected because of an unavoidable impedance mismatch in our setup. To avoid contaminating the readout signal with the reflected heater signal, we deliberately desynchronize the clock of the heater signal generator with respect to the clocks of the probe signal generator and of the digitizer. Therefore, the heater signal is averaged out from the readout signal.

For the data shown in Fig. 1c, we measure the probe transmission coefficient S_{21} to determine the normalized reflection coefficient Γ. To normalize the data, we measure a transmission coefficient S_{21}^{cal} with the gate voltage set to $V_g = -12\,V$ and with high probe and heater powers in order to move the resonance frequency of the bolometer and its tank circuit outside the frequency range considered. We note that increasing the detector temperature is an alternative way to move the resonance peak. Subsequently, we define $\Gamma = S_{21}/S_{21}^{cal}$ and fit it to an asymmetric response as in ref. [53]. Owing to, for example, reflections in the feed line, this method is known to artificially produce normalized reflection coefficients that are slightly above unity for large asymmetries, although there is no power amplification in the system. Fortunately, this feature does not affect the conclusions of this work.

Extended Data Figure 1 presents the reflection coefficient $|S_{21}|$ of the probe signal as a function of the gate voltage and the probe power. We observe that the resonance frequency can be tuned by the gate voltage by roughly 80 MHz. Nevertheless, we did not encounter spurious drifts of the resonance frequency in individual cool-downs lasting up to two months. We note that temporal fluctuations of the resonance frequency are included in the measured NEP. Change of the resonance frequency also occurs with changing probe power, where the redshift is caused by absorption of a fraction of the probe signal, which results in an increase in T_e.

We note that although the minimum NEP is observed in Fig. 3 at a vanishing gate voltage, this does not imply that the gate voltage in unnecessary. In fact, during the fabrication process the insulators in the vicinity of the graphene flake assume an unpredictable amount of static charge, which tends to shift the location of the Dirac point and other features in the terms of the gate voltage. Thus, the minimum NEP is not expected to be achieved in all devices at a vanishing gate voltage. Extended Data Fig. 1 shows that the gradient of the probe frequency with respect to the gate voltage vanishes at $V_g = 0$. Here, the effect of low-amplitude voltage fluctuations on the bolometer noise is suppressed, which may partly explain why we observe the highest sensitivity of the bolometer at a vanishing gate voltage. However, we leave the detailed study of these phenomena for future research.

Heater power calibration

To calibrate the attenuation of the heater input line shown in Extended Data Fig. 4, we placed microwave switches inside the cryostat, which allow us to effectively replace the sample with a $50\text{-}\Omega$ resistor or a direct short to the ground. By replacing the sample with a $50\text{-}\Omega$ resistor, we measure the gain of the output amplification chain up to the room-temperature mixer using the so-called Y-factor method: we connect a spectrum analyser (Rohde & Schwarz FSV 40) to this point in the chain, and measure the noise from the $50\text{-}\Omega$ resistor as a function of its temperature. Fitting a straight line to the measured power as a function of temperature yields the gain and the noise temperature of the amplification chain. For these measurements, we set the spectrum analyser resolution bandwidth to 10 MHz and take 10,000 averages. Next, we replace the sample with a direct short to the ground and measure the transmission amplitude from the heater signal generator up to the mixer using a vector network analyser with resolution bandwidth set to 10 Hz and averaging to 21. Substracting the gain of the amplification chain from the transmission measurement yields the attenuation of the heater input line, as shown in Extended Data Fig. 5

In addition to the attenuation in the heater line, the absorbed heater power is further decreased because a part of the signal is reflected from the bolometer. To account for this effect, we measure a reference transmission coefficient from the heater signal generator to the digitizer with high heating power and a gate voltage such that the resonance frequency is far from the studied frequency range; hence, the bolometer essentially fully reflects the heater tone. In addition, we measure the transmission coefficient for every data point in Fig. 3. The ratio between these data and the reference transmission coefficient yields the reflection coefficient of the bolometer for the heater tone, Γ_h, from which we obtain the absorbed fraction of the heater power reaching the bolometer as $1 - |\Gamma_h|^2$. The absorbed heater power is obtained by multiplying the heater power applied at the generator by this fraction and by the measured attenuation of the heater line. The absorbed heater power is used in all measurements of the responsivity of the detector. This is justified because it is straightforward to engineer an essentially perfectly impedance-matched heater line to this type of bolometer, as shown in refs. [13,33].

Although we leave the impedance matching for future work, we note that our sample has a separate heater junction and line defined (see unused structures in Fig. 1), which implies that we do not expect the performance of the bolometer to degrade once the impedance-matched absorber is finalized and functional; namely, we do not need to change the size or number of gates on the graphene.

However, a band-pass filter at the input of the bolometer is advantageous because without filtering, an impedance-matched input line gives rise to photonic heat conduction equal to a quantum of thermal conductance, and consequently the NEP of the bolometer may increase owing to the limit imposed by thermal fluctuations, NEP_{TEF}. According to our calulations, a third-order elliptic 1-GHz band-pass filter provides $NEP_{TEF} = 10$ zW Hz$^{-1/2}$ at 50 mK. Thus, the bolometer has potential to operate with ultralow noise and a broad absorption band.

Differential thermal conductance

The differential thermal conductance of an electron system at temperature T_e is defined as the partial derivative $\partial P_{eb}/\partial T_e$ of the heat flowing out of the electron system into its bath at temperature T_b. Here, the derivative is taken with respect to the electron temperature such that the bath temperature is constant. Owing to the small size of the graphene flake, however, the measurement of T_e in our system has a large uncertainty, for example, due to parasitic heat contributions that may dominate at temperatures below 50 mK. Therefore, we instead compute the differential thermal conductance from

$$\widetilde{G} = -\partial P_{e-b}(T_e, T_b)/\partial T_b$$

where the electron temperature is considered constant. This is valid as long as we consider linear channels for the flow of the heat currents[33,54], with no rectification.

In Fig. 1d, we show the thermal model for heat transfer between T_e and T_b. The differential thermal conductance $\widetilde{G}$ is a sum of three contributions: the electron–phonon coupling, G_{ep}, the electron diffusion into the superconducting leads, G_{diff}, and the electromagnetic coupling with the environment, G_{photon}. For simplicity, we consider the conveniently measurable cryostat bath temperature, T_b, to coincide with the temperatures of all baths directly coupled to the electron system of the graphene flake. Thus, the thermal effects of the system are effectively described by a single heat capacity C_e directly coupled to the cryostat phonon bath with a thermal conductance $\widetilde{G}$. Our observations in Fig. 2c of a single thermal time constant τ support the validity of this simple thermal model.

We note that we thermalized the sample holder well to the mixing-chamber plate of the cryostat by applying force using well tightened screws to keep the two gold-plated surfaces tightly together. Thus, the sample holder assumes a temperature very close to that of

the cryostat bath down to the lowest temperature of 50 mK used in this study. According to the specifications of the manufacturer, the uncertainty of the used RuO$_2$ thermometer is 4 mK at 50 mK bath temperature.

The method that we use to obtain $\widetilde{G}$ is based on mapping the contours of a constant monotonically T_e-dependent quantity $A(T_e)$ in the T_b–P_{appl} plane and taking a derivative of the contour[54], thus satisfying the above condition that the electron temperature must be constant. Here, we choose the resonance frequency as the T_e-dependant quantity because it decreases monotonically with increasing electron temperature.

In practice, we measure the contours of constant resonance frequency by searching for the heater power required to keep the resonance frequency constant given a change in the bath temperature (Fig. 2a). This is a slow measurement because we need to change the temperature of the whole mixing-chamber plate of the cryostat, which consists of several kilograms of metal. Consequently, the measurement is affected by significant $1/f$ noise. Although the effect of this noise is reasonable in the contours of constant electron temperature in Fig. 2a, its relative contribution would become too large if we took a simple numerical derivative of the contours to obtain the differential thermal conductance. Therefore, we instead make a polynomial fit to the data in Fig. 2a and differentiate the fitted function. In Fig. 2b we show these results along with power-law fits to the differential thermal conductances, motivated by this kind of typical behaviour in the heat conduction channels.

Extraction of the regime of linear response

Our definition of NEP assumes that the response of the detector is linear with respect to the heater power, that is, the responsivity of the detector is constant. Therefore, we measure the response as a function of heater power at the (P_p, f_p) point, where we find the lowest NEP for each gate voltage. The results are shown in Extended Data Fig. 6. We find a linear response of up to 16 aW with −2.5 V gate bias, and 4 aW with 0 V and 2.5 V bias.

Data acquisition and processing

In our previous work with metallic proximity Josephson junctions[55], we noticed that losses in the junction may increase with the frequency increasing above 500 MHz. For the tank circuit of the bolometer, excessive losses may lead to boadening of the probe resonance, and consequently to loss of responsivity. Thus, we choose to work in this 500-MHz frequency range for the probe signal. However, full optimization of the probe frequency over many decades has the potential to provide future improvements of the performance of the bolometer.

After reflection from the bolometer, amplification and filtering, the 500-MHz probe signal is converted down to 70.3125 MHz by the analogue electronics shown in Extended Data Fig. 4. This intermediate-frequency signal is digitized at a rate of 250×10^6 samples per second by an NI-5782 analogue-to-digital converter connected to an NI-7972R field-programmable gate array (FPGA). The recorded samples are digitally down-converted to d.c. on the FPGA. Owing to technical limitations, our FPGA runs at a clock frequency of 125 MHz, and therefore we perform the down-conversion to two samples in parallel. Consequently, we obtain both the in-phase (I) and quadrature (Q) signals for both the probe and the reference channel, resulting in a total of eight channels of data. Subsequently, we combine the two parallel samples owing to bring the total number of data channels down to four. We also have the option to combine temporally adjacent samples on the FPGA. Typically we combine four samples in total, so the effective digitization rate is 62.5×10^6 samples per second. The FPGA collects a pre-determined number of samples and also carries out ensemble-averaging of all four data channels. For the data presented in Fig. 3, we took 262,144 ensemble averages for the time traces, and the noise spectrum was averaged over 30 repetitions. For the linearity measurements presented in Extended Data Fig. 6, we took 32,768 averages.

Article

After the averaging, the data are transferred to a desktop computer. We rotate the I and Q signals so that the bolometer response appears completely in the in-phase signal I. For technical reasons, we further apply a digital low-pass filter to the data with a cut-off frequency of 2 MHz. Figure 2c shows the filtered signal in a typical experiment in which we apply a heater pulse to the bolometer for a certain period of time to measure the thermal time constant and d.c. response. To this end, we fit an exponential function to the filtered data separately for the rising and the falling edges because the time constant of the edges can, in general, be different owing to electrothermal feedback. In the NEP and energy resolution calculation, we use the time constant obtained for the rising edge. For the differential thermal conductance data presented in Fig. 2a, b, we took 16,384 averages.

Data availability

Data supporting the findings of this study are available at https://zenodo.org/record/3978419.

Code availability

The algorithms used for the findings of this study are available within the paper and its Supplementary Information files.

51. Du, X., Prober, D. E., Vora, H. & Mckitterick, C. B. Graphene-based bolometers. *Graphene 2D Mater.* **1**, 1–22 (2014).
52. Song, X. et al. Stamp transferred suspended graphene mechanical resonators for radio frequency electrical readout. *Nano Lett.* **12**, 198–202 (2012).
53. Geerlings, K. et al. Improving the quality factor of microwave compact resonators by optimizing their geometrical parameters. *Appl. Phys. Lett.* **100**, 192601 (2012).
54. Govenius, J. et al. Microwave nanobolometer based on proximity Josephson junctions. *Phys. Rev. B* **90**, 064505 (2014).
55. Lake, R. E. et al. Microwave admittance of gold-palladium nanowires with proximity-induced superconductivity. *Adv. Electron. Mater.* **3**, 1600227 (2017).

Author contributions R.K. and J.-P.G. conducted the experiments and data analysis of the data presented in the main article. The main sample was designed by R.E.L. and fabricated by D.H. and A.L. Initial characterizations were carried out by I.S., D.H. and J.G. Most of the measurement code was written by V.V. and J.G. Furthermore, J.Y.T. and K.W.C. fabricated the sample discussed in Supplementary Note I, which was measured and analysed by M.P. and K.Y.T. The sample presented in Supplementary Note II was produced by R.E.L. and A.L., and measured mainly by J.G. The manuscript was written by R.K., J.-P.G. and M.M. with comments from all authors. The work was supervised by P.H. and M.M.
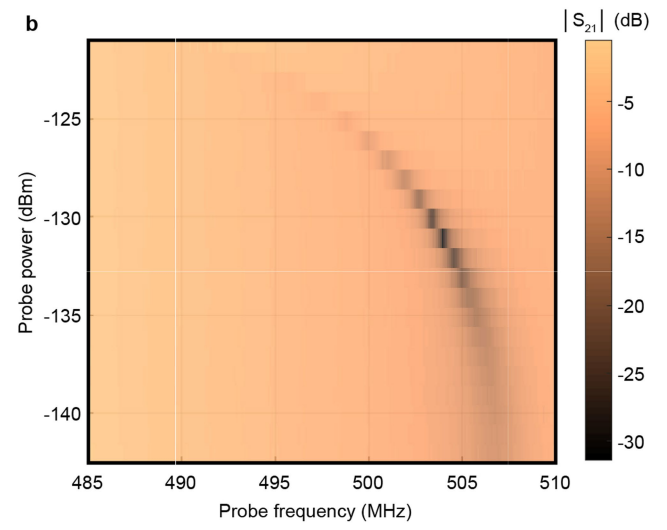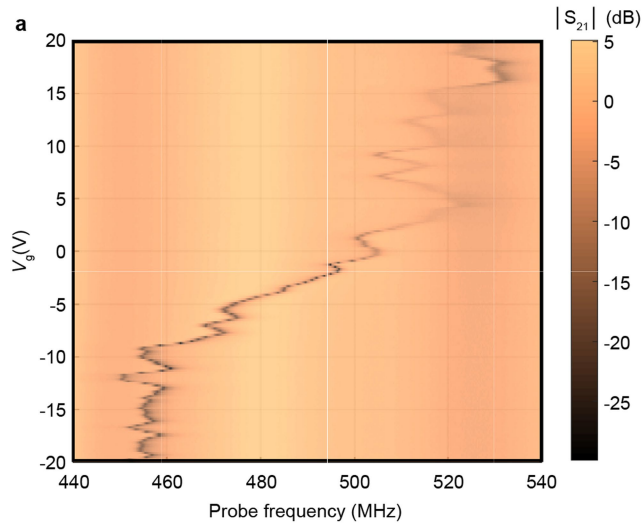
Extended Data Fig. 1 | Controlled shift of the resonance frequency.
a, Measured reflection amplitude of the bolometer as a function of the probe frequency and the gate voltage at $P_p = 17.4$ aW. **b**, Reflection amplitude as a function of the probe frequency and power at $V_g = 0$ V. In each panel and each horizontal trace, the point of the lowest reflection amplitude roughly yields the resonance frequency. The bath temperature is $T_b = 55$ mK and no heater power is applied.
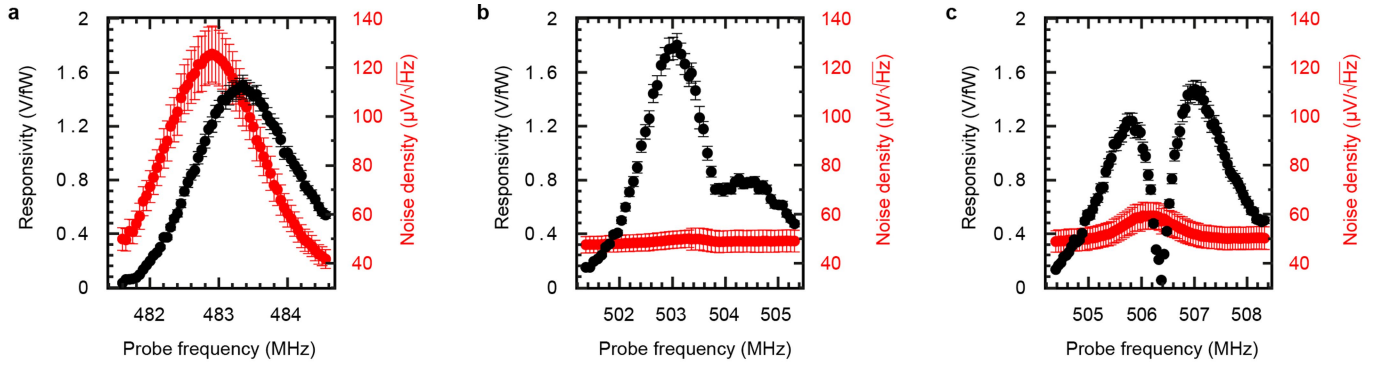
Extended Data Fig. 2 | Responsivity and average noise density. a–c, Quasistatic responsivity (black markers, left axis) and noise density averaged over the frequency range 10^2–10^4 Hz (red markers, right axis) as functions of the probe frequency for gate voltages −2.5 V (**a**), 0 V (**b**) and 2.5 V (**c**). Dividing the noise density with the responsivity yields the NEP shown in Fig. 3. The bath temperature is $T_b = 55$ mK.
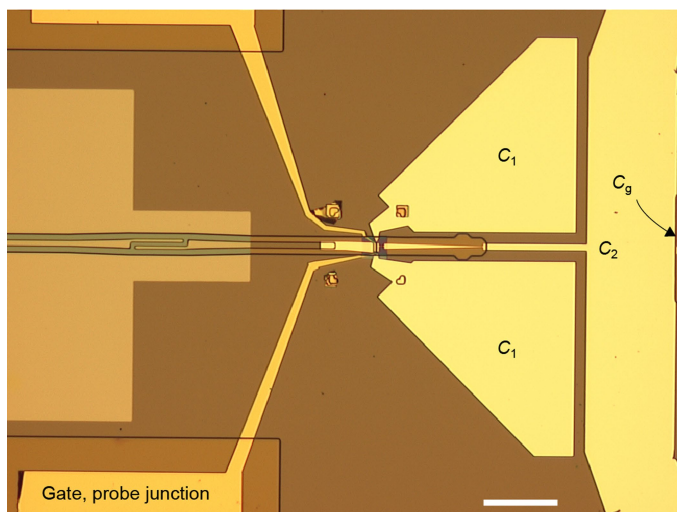
Extended Data Fig. 3 | On-chip details of the bolometer. Optical image of the bolometer, indicating the locations of capacitors C_1, C_2 and C_g. The transmission line at the centre left and the absorber gate line at the top left were not used in the experiment. The scale bar denotes 100 μm.

Article
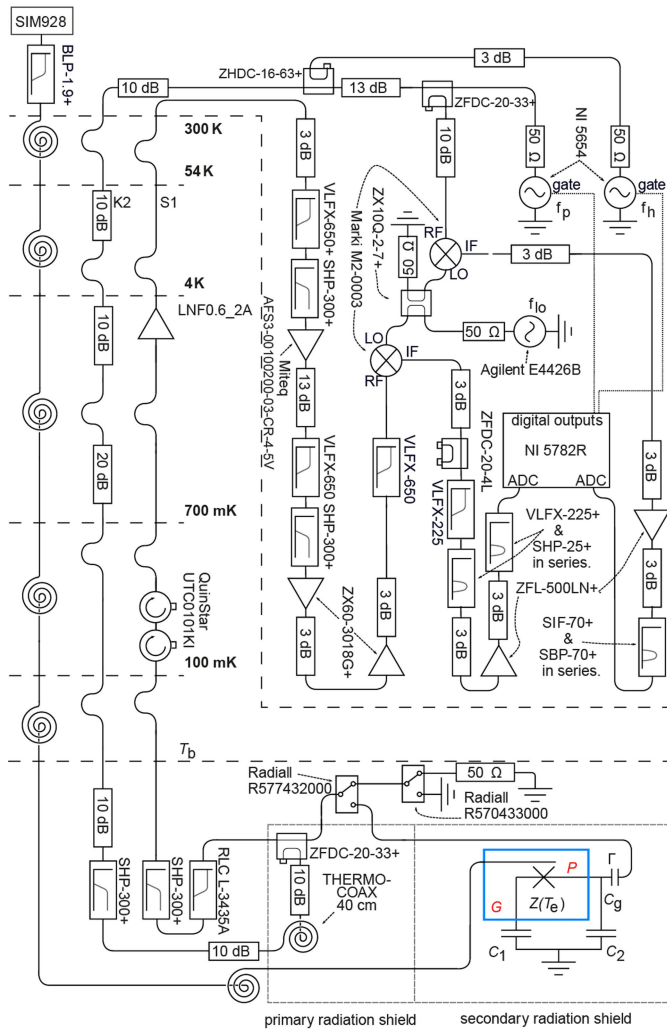
Extended Data Fig. 4 | Detailed measurement setup. The blue rectangle corresponds to the SEM image displayed in Fig. 1a. The model numbers on the filters, couplers and amplifiers refer to Mini-Circuits product numbers. Nominal temperatures of the different cryostat plates (dashed horizontal lines) are indicated. The 180° bends and spirals refer to long segments in the coaxial microwave cables and Thermocoax cables, respectively, which function as thermal bottlenecks separating the different temperature stages. The top-most dashed line refers to the boundary of the cryostat. The nested millikelvin radiation shields are made of gold-plated copper.
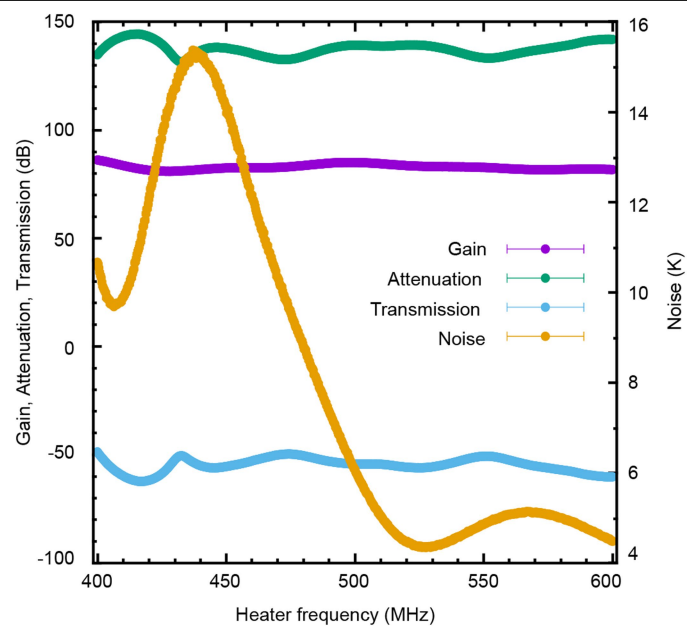
Extended Data Fig. 5 | Calibration of the heater power. Gain (left axis) and noise temperature (right axis) of the amplification chain from the microwave switch shown in Extended Data Fig. 4 to the room-temperature mixer, transmission amplitude from the heater signal generator to the mixer (left axis), and attenuation of the heater line from the signal generator to the switch (left axis) as functions of heater frequency. The error bars denote 1σ confidence intervals.
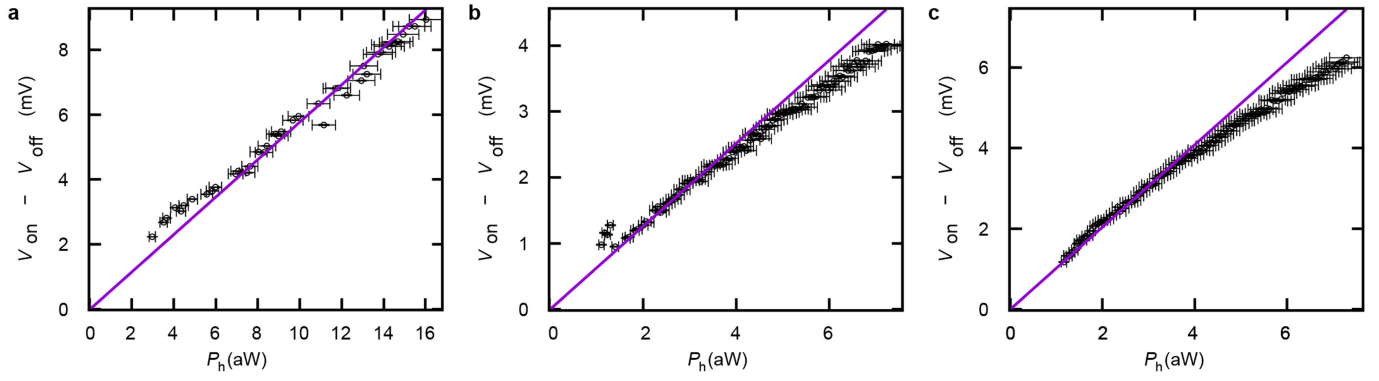
Extended Data Fig. 6 | Response to heater power. a–c, Difference in the voltage of the measured probe signal quadrature between heater-on and heater-off conditions as a function of the heater power level in the on state for gate voltage −2.5 V (**a**), 0 V (**b**) and 2.5 V (**c**) at the probe power and frequency for which we find the lowest NEP in Fig. 3. The solid line shows a linear fit up to a heating power of 16 aW (**a**) and 4 aW (**b**, **c**). The error bars denote 1σ confidence intervals.

a

b
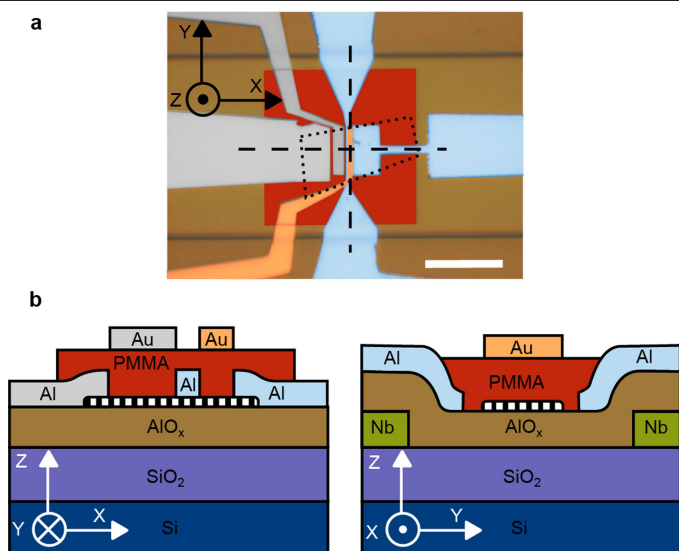
Extended Data Fig. 7 | Schematic cross sections of the bolometer. a, Optical image of the bolometer. Grey colour indicates unused structures in our experiment. The boundary of the graphene flake is denoted by the dotted quadrangle. The scale bar denotes 5 μm. **b**, Schematic cross-sections of the bolometer along the dashed lines of the optical image (not to scale).

Extended Data Table 1 | Parameters of the polynomial fitting function $P_{\mathrm{appl}} = [p_1(T_\mathrm{b}/K)^3 + p_2(T_\mathrm{b}/K)^2 + p_3 T_\mathrm{b}/K + p_4]$ fW for Fig. 2a

Gate voltage / Fit parameter	p_1	p_2	p_3	p_4
V_g = -2.5 V	-7.14	-6.07	-0.90	0.30
V_g = 0 V	-6.22	-5.64	-0.11	0.17
V_g = 2.5 V	6.83	-11.1	-0.26	0.37